


PAPER

[View Article Online](#)
[View Journal](#) | [View Issue](#)Cite this: *Mater. Adv.*, 2022,
3, 5151Amine-functionalized stable Nb₂CT_x MXene
toward room temperature ultrasensitive
NO₂ gas sensor†Arkoti Naveen Kumar^a and Kaushik Pal  ^{*ab}

Large surface area and abundant surface functional groups favor the MXene (Nb₂CT_x) for potential gas sensor applications. However, atmospheric instability is the major limitation of MXenes. In this work, (3-aminopropyl)triethoxysilane (APTES) with distinct concentrations (0.1, 0.2, 0.3 mL) was used for the surface modification of MXene, which is a popular silane coupling agent. It minimizes the oxidation of the MXene by forming a homogeneous, thick protective layer on the Nb₂CT_x MXene structures by covalent contact through silylation processes, thereby allowing the simultaneous incorporation of additional reactive groups (–NH₂). The functionalization and stability of the synthesized materials were characterized using XRD, FESEM, HR-TEM, XPS, FT-IR, UV-Vis, and zeta potential. The hydrophilic –NH₂ group acts as an electron donor that helps sense acidic gases such as nitrogen dioxide (NO₂). APTES-functionalized Nb₂CT_x MXene showed a better sensing response toward NO₂ gas (31.52%) than pristine Nb₂CT_x MXene (12.5%) at 25 ppm, which is stable for more than 45 days at room temperature (~25 °C). The sensitivity of Nb₂CT_x and Nb₂CT_x-0.2 APTES MXene shows 0.492 and 1.2314 ppm^{–1}, respectively, confirming that APTES-functionalized Nb₂CT_x MXene shows better sensitivity. Nb₂CT_x-0.2 APTES sensors can sense the NO₂ gas at the detection limit (LOD) of 3 ppb and quantification limit (LOQ) of 12 ppb. In contrast, the pristine Nb₂CT_x sensor can provide an LOD of 15 ppb and LOQ of 52 ppb, showing that the APTES-functionalized Nb₂CT_x sensor can sense even a minute concentration of the gas with high sensitivity.

Received 16th March 2022,
Accepted 17th May 2022

DOI: 10.1039/d2ma00301e

rsc.li/materials-advances

Introduction

The necessity for the selective and sensitive detection of toxic gases and volatile organic compounds (VOCs) in food quality control, environmental monitoring, industrial process management, medical diagnostics, and occupational safety has increased in recent years.¹ Nitrogen dioxide (NO₂) is one of the major pollutants along with other toxic gases such as CO₂, NH₃, SO₂, and CO. NO₂ is a flammable, colorless gas released from industrial productions and automotive emissions, leading to the damage to the ozone layer and causing acid rains.² Moreover, when the concentration of NO₂ gas exceeds 410 parts per billion (ppb) in an hour and 82 ppb in a year in the air, it leads to significant health issues, as stated by the World Health Organization (WHO).³ Chemiresistive-type sensors have been extensively employed to detect these toxic gases, compared to

potentiometric, calorimetric, catalytic, conductometric type sensors due to high sensitivity, selectivity, simplicity in fabrication, low cost, less power consumption, and low operating temperatures.⁴

For a typical resistive-type sensor, two significant parameters should be considered simultaneously, such as (i) high signal induced by strong and abundant analyte adsorption sites and (ii) low electrical noise induced by high conductivity.⁵ Metal oxide semiconductor materials are majorly used for chemiresistive-based sensors because of their high sensitivity, long-term stability, and fast response. However, they have limitations in terms of low electrical conductivity and high operating temperatures.⁶ In recent years, researchers have been working on various two-dimensional nanomaterials that show high surface-to-volume ratios, nanoscale thickness, and outstanding surface tunability.⁷ 2D nanomaterials including graphene,⁸ nanobelts,⁹ phosphorene,¹⁰ and TMDs (Transition Metal Dichalcogenides)¹¹ are extensively studied for sensing different toxic gases. Another 2D material called MXene is being studied in the recent years due to its high metallic conductivity and abundant surface functional groups.

MXene is a new class of fast-growing 2D transition metal carbides/nitrides synthesized by selectively etching A group (usually IIIA and IVA group elements) from the layered MAX

^a Centre for Nanotechnology, Indian Institute of Technology Roorkee, Roorkee, 247667, India. E-mail: pl_kshk@yahoo.co.in, kaushik@me.iitr.ac.in; Fax: +91-1332-285665; Tel: +91-1332-284761

^b Department of Mechanical and Industrial Engineering, Indian Institute of Technology Roorkee, Roorkee, 247667, India

† Electronic supplementary information (ESI) available. See DOI: <https://doi.org/10.1039/d2ma00301e>

phase. The general expression for MXene is $M_{n+1}X_nT_x$, where M is early transition metals, X is carbides/nitrides with $n = 1, 2$, or 3 , and T_x is the surface terminations such as $-O$, $-OH$, and $-F$.¹² MXenes have excellent applications in energy harvesting,¹³ energy storage,¹⁴ photo/electrocatalysts,¹⁵ water purification,¹⁶ and sensors¹⁷ due to the excellent properties of MXenes, such as high metallic conductivity (results in low noise), surface functional groups (results in strong binding of analytes), and high specific surface area (results in high signal to noise ratio). Recently, $Ti_3C_2T_x$, V_2CT_x , MoC_{1-x} MXenes have been studied experimentally for gas sensing applications^{18,19} and other MXenes were studied theoretically.²⁰ γ -Poly(L-glutamic acid) (γ -PGA) was used to modify the $Ti_3C_2T_x$ MXene to improve the gas sensing performance. The response of modified $Ti_3C_2T_x$ MXene shows a sensing response that is 85% stronger than that of pristine $Ti_3C_2T_x$ MXene at 50 ppm NO_2 gas.²¹ Alkalized V_2CT_x MXene with accordion-like structure was synthesized by mild etching, followed by alkaline treatment. The alkalized V_2CT_x MXene showed 80 times stronger response than pristine V_2CT_x MXene at 50 ppm NO_2 gas.²² Nb_2CT_x MXene was also studied for gas sensing in recent years experimentally²³ due to the large surface area compared to $Ti_3C_2T_x$ MXene. The large surface area allows for an increase in the charge transfer in the sensing device.

The thermodynamic instability of the exfoliated MXene in water and oxygen environment leads to the formation of highly stable metal oxides and hence leads to the loss of high electrical conductivity that hinders the application in gas sensing.²⁴ Surface treatment is a feasible method for increasing MXene's stability.²⁵ (3-Aminopropyl)triethoxysilane (APTES) is a common silane coupling reagent that decreases MXene oxidation while allowing the simultaneous insertion of additional reactive groups ($-NH_2$). The surface modification of APTES on MXene may have four possible types of interactions. APTES adsorbs on hydroxyl-terminated MXene through oxygen bonding from one, two, or three ethoxy groups by forming ethanol as a by-product. The bonding of three ethoxy groups on the MXene surface may lead to the polymerization of adsorbed APTES by forming siloxane bonds ($Si-O-Si$). The fourth possible APTES adsorption is *via* amino group on the hydroxyl surface of MXene. APTES adsorption on the MXene surface is rather complex and still not understood in detail.²⁶ After the intermolecular hydrolysis process, the produced silanol groups can engage with surface hydroxide radicals to create covalent bonds.²⁷ The amine functional groups on APTES donate an electron and help to detect acidic gases such as CO_2 , NO_2 , and SO_2 . To the best of our knowledge, there is no literature available for APTES-functionalized Nb_2CT_x MXene on gas sensor applications. Herein, we report the synthesis, characterization, and testing of pristine and functionalized MXene for its long-term stability and gas sensing.

Experimental section

Materials

Nb_2AlC MAX phase was obtained from Jilin 11 technology Co., Ltd, China. Hydrofluoric acid (48%) was purchased from

Avantor Performance Materials India Limited, India. (3-Aminopropyl)triethoxysilane (APTES) was procured from SRL Pvt. Ltd, India. Tetramethylammonium hydroxide (TMAOH, 25% aq. solution) was acquired from Molychem, India. De-ionized water was obtained with 18.2 M Ω cm resistivity and used during synthesis. All the materials were used as received without any further purification.

Nb_2CT_x synthesis procedure

Herein, we synthesized Nb_2CT_x MXene from the Nb_2AlC MAX phase by etching out the Al, as published elsewhere²⁸ with slight modifications. In a typical procedure, we took 0.5 g of Nb_2AlC in 10 mL of 48% hydrofluoric acid and stirred for 48 h at 55 °C. The obtained mixture was centrifuged at 3500 rpm for 5 min and the supernatant was decanted. The same procedure was repeated till the pH of the mixture reached 7. The resulting sample was dried in a vacuum desiccator overnight. To perform the delamination of MXene, the dried sample was immersed in 20 mL of DI water, and 1 mL of tetramethylammonium hydroxide (TMAOH, 25% aqueous solution) was added to the MXene solution and kept for 12 h stirring at room temperature. The sample was centrifuged with DI water at 5000 rpm for 30 min till the pH became neutral. 50 mL of DI water was added to the delaminated MXene sample and sonicated for 1 h under Ar atmosphere. The resulting solution was centrifuged at 5000 rpm for 1 h, and the supernatant was collected. The final MXene sample was centrifuged at 12 000 rpm for 30 min, and the sedimented sample was dried in a vacuum desiccator at room temperature for 24 h. The obtained powder was used for further modification and testing.

Nb_2CT_x -amine functionalization procedure

0.1 g of Nb_2CT_x MXene was dispersed in a water and ethanol mixture of 1:9 ratio in three different poly bottles to provide enough water for a hydrolysis reaction. Subsequently, three different concentrations of APTES (0.1 mL, 0.2 mL, and 0.3 mL) were added to the above mixture. The solution was stirred at 400 rpm for 8 h under nitrogen bubbling. Subsequently, the obtained solution was cleaned with ethanol 5–6 times to remove unreacted APTES by centrifugation. The obtained sedimented slurry was dried in a vacuum desiccator at room temperature for 24 h (Fig. 1). The obtained final sample was used for further characterization and testing.

Characterization techniques

A Rigaku smart lab XRD with CuK_α radiation (1.54 Å) was used for structural analysis of all the prepared samples. The prepared samples were studied for morphology and composition by a field emission scanning electron microscope (Carl-Zeiss, Zeiss GeminiSEM) with energy dispersive spectroscopy and transmission electron microscopy (JEM 3200FS electron microscope). Functional groups and chemical oxidation studies were performed on a Fourier transform infrared spectrometer (Thermo Nicolet spectrometer) and X-ray photoelectron spectrometer (PHI 5000 VersaProbe III). Stability analysis of the prepared samples was performed with an Agilent Cary 60 UV-Vis



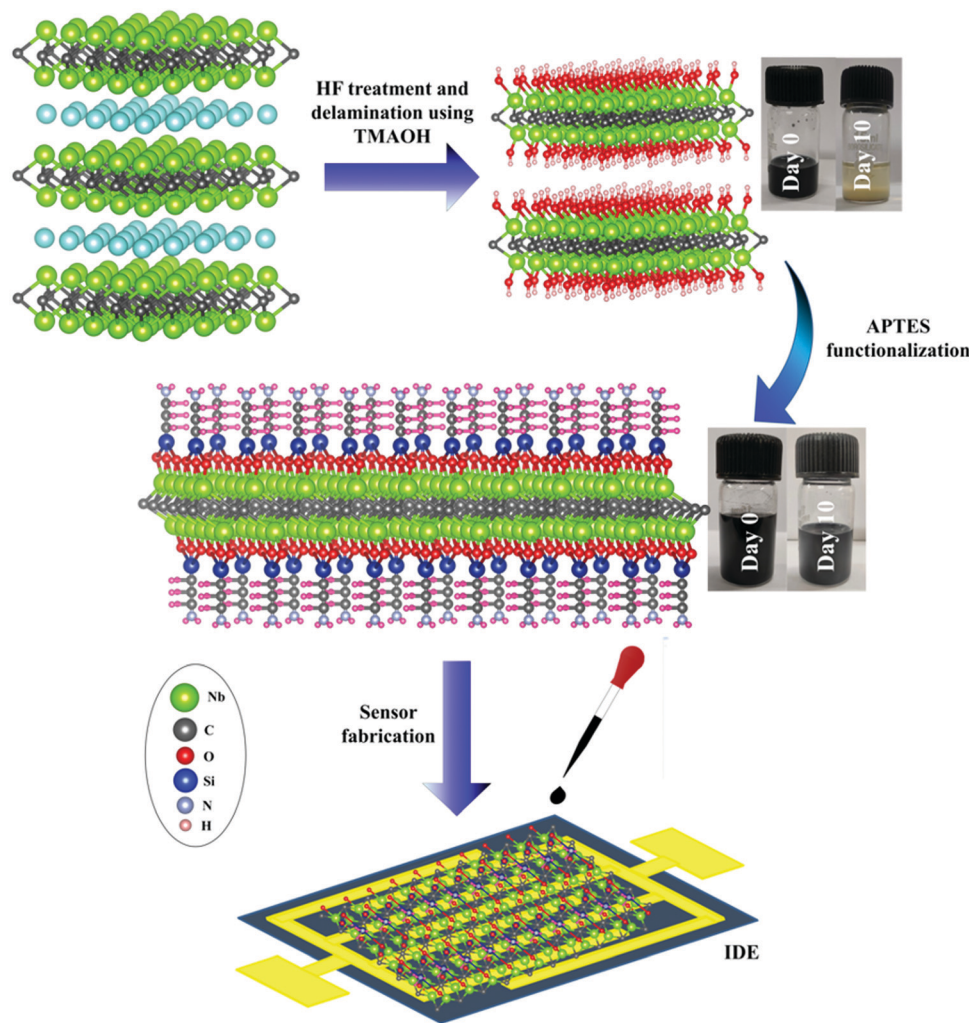


Fig. 1 Schematic representation of synthesis and sensor fabrication of Nb_2CT_x and $\text{Nb}_2\text{CT}_x\text{-APTES}$ MXene.

Spectrophotometer and zeta potential (Malvern Instruments, USA). The specific surface areas of the samples were determined by the gas sorption technique using a Quantachrome Nova Gas Sorption Analyzer based on the Brunauer–Emmett–Teller (BET) method.

Fabrication of the sensor and experimental setup

Interdigitated electrodes (IDEs) were used in the preparation of all the sensors. The fabrication of IDEs was as follows from our recently published work.²⁹ IDEs were initially cleaned with ethanol, DI water, and isopropyl alcohol for 5 min each in a bath sonicator and dried. After drying, we performed the soldering of Cu wire for electrical connections using a soldering gun. The silver paste was used to increase the Cu wire and IDE connection. We used a binder (Bondtite, high strength compound) to increase the soldering strength. 1–2 μL of Nb_2CT_x , APTES-functionalized Nb_2CT_x MXene, was drop-cast on the developed IDE and dried in a vacuum desiccator at room temperature overnight for sensor fabrication (Fig. 1). The fabricated sensor was transferred to a self-designed testing chamber connected to mass flow controllers (MFCs; 5850E, Brooks Instrument) and two electrodes. The copper

electrical wires of the sensor were connected to the electrodes provided on top of the self-designed testing chamber, which is connected to a digital picoammeter (DPM-111, SES Instruments Pvt. Ltd, Roorkee), by which the change in the resistance of the gas was measured. The MFCs were used to control the gas flow (such as dry air, NO_2 , CO_2 , and NH_3) into the testing chamber to maintain the desired gas concentration. The experiments were carried out at a bias of 1 V through a DC power supply unit (L-3210, Aplab, India). Initially, the sensor was exposed to dry air (79% N_2 and 21% O_2) for 20 min to stabilize and measure the baseline resistance. Later, the sensor was exposed to NO_2 gas at different concentrations through computer-controlled MFCs (5 to 25 ppm), and the response was automatically recorded in the data recording system (computer). The selectivity test of the sensor was performed with CO_2 , NH_3 , ethanol, acetone, methanol, isopropyl alcohol, and chloroform. Dry air was purged every time to get the baseline resistance for every different gas tested. The sensor response was calculated using the formula³⁰

$$\left(\frac{\Delta R}{R_a}\right)\% = \frac{R_g - R_a}{R_a} \times 100 \quad (1)$$



where, R_a and R_g are known as the resistances of dry air and target gas, respectively. The response and recovery times are defined as the time taken to reach 90% of the electrical resistance change for the adsorption and desorption of gases.

Results and discussion

FTIR and XPS were used to analyze the changes in the surface chemical states of the before and after the functionalization of Nb_2CT_x MXene samples. The FTIR spectrum depicted in Fig. S1 (ESI[†]) corresponding to APTES-functionalized MXene shows asymmetric and symmetric vibrations of the C–H group at 2929 and 2863 cm^{-1} compared to that of pristine MXene. The band at 1620 cm^{-1} in Fig. S1(c–e) (ESI[†]) characterizes the primary amine stretching vibration, which can be the evidence of functionalization of APTES onto MXene.²⁷ Si–O–Nb, Si–O–C, and Si–O–Si stretching bands fall in the wavenumber range of 810–1190 cm^{-1} . The decrease in –OH stretching in Fig. S1(c–e) (ESI[†]) compared to Fig. S1(b) (ESI[†]) further confirms the APTES functionalization on Nb_2CT_x MXene.²⁵

Fig. 2(a–d) shows the high-resolution XPS spectrum of C 1s, Nb 3d, O 1s, and N 1s of pristine Nb_2CT_x MXene; (e–h) shows the high-resolution XPS spectrum of C 1s, Nb 3d, O 1s, and N 1s of the as-synthesized APTES-functionalized Nb_2CT_x MXene. Fig. S2(a–d) (ESI[†]) shows the high-resolution XPS spectrum of C 1s, Nb 3d, O 1s, and N 1s of Nb_2CT_x MXene; (e–h) shows the high-resolution XPS spectrum of C 1s, Nb 3d, O 1s, and N 1s of the as-synthesized APTES-functionalized Nb_2CT_x MXene after 15 days. The survey spectrum in Fig. S3 (ESI[†]) shows the Nb 3d, C 1s, O 1s, F 1s, N 1s, and Si 2s elements before and after degradation. From the normalized intensities of the prepared materials in Fig. S3 (ESI[†]), it can be concluded that pristine Nb_2CT_x MXene degraded more than APTES-functionalized Nb_2CT_x MXene. This is due to the hydrophobic silane group of APTES attached on Nb_2CT_x MXene that stops the interaction of oxygen or water molecules from the environment. Table S1 (ESI[†]) shows the atomic concentrations of the prepared samples for the confirmation of degradation. The Nb–C bond at 281.5 eV of the C 1s spectrum shown in Fig. 2(a) vanished entirely after 15 days of Nb_2CT_x MXene into the atmosphere (see C 1s XPS spectrum of Fig. S2(a), ESI[†]). However, the Nb–C bond at 281.1 eV is still present even after 15 days for APTES-functionalized Nb_2CT_x MXene, as shown in Fig. S2(e) (ESI[†]). The degradation is also confirmed from the Nb–C bond present at 204.6 eV in Fig. 2(b) and the absence of the same in Fig. S2(b) (ESI[†]) of the Nb 3d spectrum. The intensity of the Nb_2O_5 peak at 530 eV in Fig. 2(c and g) and Fig. S2(c and g) (ESI[†]) confirms that less oxidation has been observed on APTES-functionalized Nb_2CT_x MXene. The N 1s high-resolution XPS spectrum shown in Fig. 2(h) was used to determine the protonation states of the amino groups on the surface of Nb_2CT_x -APTES MXene. The spectrum was deconvoluted into two different peaks of free amine and protonated amine with respective binding energies of 399.8 and 402.0 eV. This confirms the attachment of the amine groups on Nb_2CT_x MXene that help in sensing acidic gases.

XRD studies were conducted to understand the phase structure of the synthesized pristine Nb_2CT_x MXene, APTES-functionalized Nb_2CT_x MXene, and Nb_2AlC MAX phase. All the pristine and synthesized samples showed highly crystalline structure and purity comparable with the JCPDS card details of (JCPDF 15-0127). The major peaks in the MAX phase at $2\theta = 38.8^\circ$, which is attributed to the presence of aluminum, vanished completely in the MXene phase, and another prominent peak at $2\theta = 12.9^\circ$ attributed to the (002) peak of the MAX phase got shifted to $2\theta = 7.06^\circ$ in the MXene phase that confirms the complete formation of the MAX phase into MXene, as shown in Fig. 3(A and B). ϵ weak bonding between the Nb–Al bond compared to the Nb–C bond helped in the selective removal of the Al layer by HF treatment at a higher temperature. Water molecules intercalate between the sheets during the washing process due to weaker hydrogen bonding in the M–Al layers than stronger metallic bonds. Thus, hexagonally stacked 2D sheets of Nb_2CT_x MXene were formed due to relative bond strength among the elements. The XRD peaks near 33.6 degrees correspond to the (1 0 0) plane and 59.9 degrees correspond to the (1 1 0) plane of Nb_2C MXene (JCPDS 15-0127), which is consistent with the previously reported diffraction peaks.³¹ The d -spacing values were calculated to be 12.47, 12.52, 12.59, and 12.65 Å for Nb_2CT_x , Nb_2CT_x -0.1 APTES, Nb_2CT_x -0.2 APTES, and Nb_2CT_x -0.5 APTES MXenes, respectively. APTES has been used in this study to improve the stability. However, a slight change in the interlayer spacing was observed with an increase in the APTES concentration in the MXene, indicating that the surface was effectively functionalized with APTES, which offers protection from the spontaneous oxide formation of MXene in ambient water and oxygen.

The morphology and structural studies of the synthesized samples were characterized using FE-SEM and TEM analyses. The Nb_2AlC MAX phase (Fig. S4, ESI[†]) was etched on Nb_2C MXene by HF-TMAOH and ultrasonication process. Compared with Nb_2C MXene, APTES-functionalized MXene stays intact in structure with little higher exfoliation, as shown in Fig. 4(a and c). Elemental mapping [Fig. 4(b and d)] shows that the two new elements of N and Si in functionalized MXene offers the successful grafting of APTES on MXene. TEM and high-resolution TEM (HR-TEM) (Fig. S5, ESI[†]) show the exfoliation of the pristine and 0.2 APTES-functionalized Nb_2CT_x MXene. The SAED pattern shows the crystallinity of the synthesized samples. The surface area of the prepared samples was characterized by BET analysis. Table S2 (ESI[†]) provides the surface area, pore volume, and pore width values of the pristine Nb_2CT_x and Nb_2CT_x -0.2 APTES-functionalized MXene. The surface area of 40.892 and 49.377 $m^2 g^{-1}$ was recorded for pristine Nb_2CT_x and Nb_2CT_x -0.2 APTES functionalized MXene, respectively.

Degradation over time is the major challenge that MXene faces in the water and dissolved oxygen environment. It results in the conversion of MXene into its corresponding metal oxides and a reduction in its conductivity.³² UV-Vis analysis was used to study the degree of degradation of pristine and functionalized MXene. For comparison, the absorbance values of pristine and functionalized MXene were taken at 400 nm. From Fig. S7 (ESI[†]), the stability of the MXene was shown to increase as the APTES



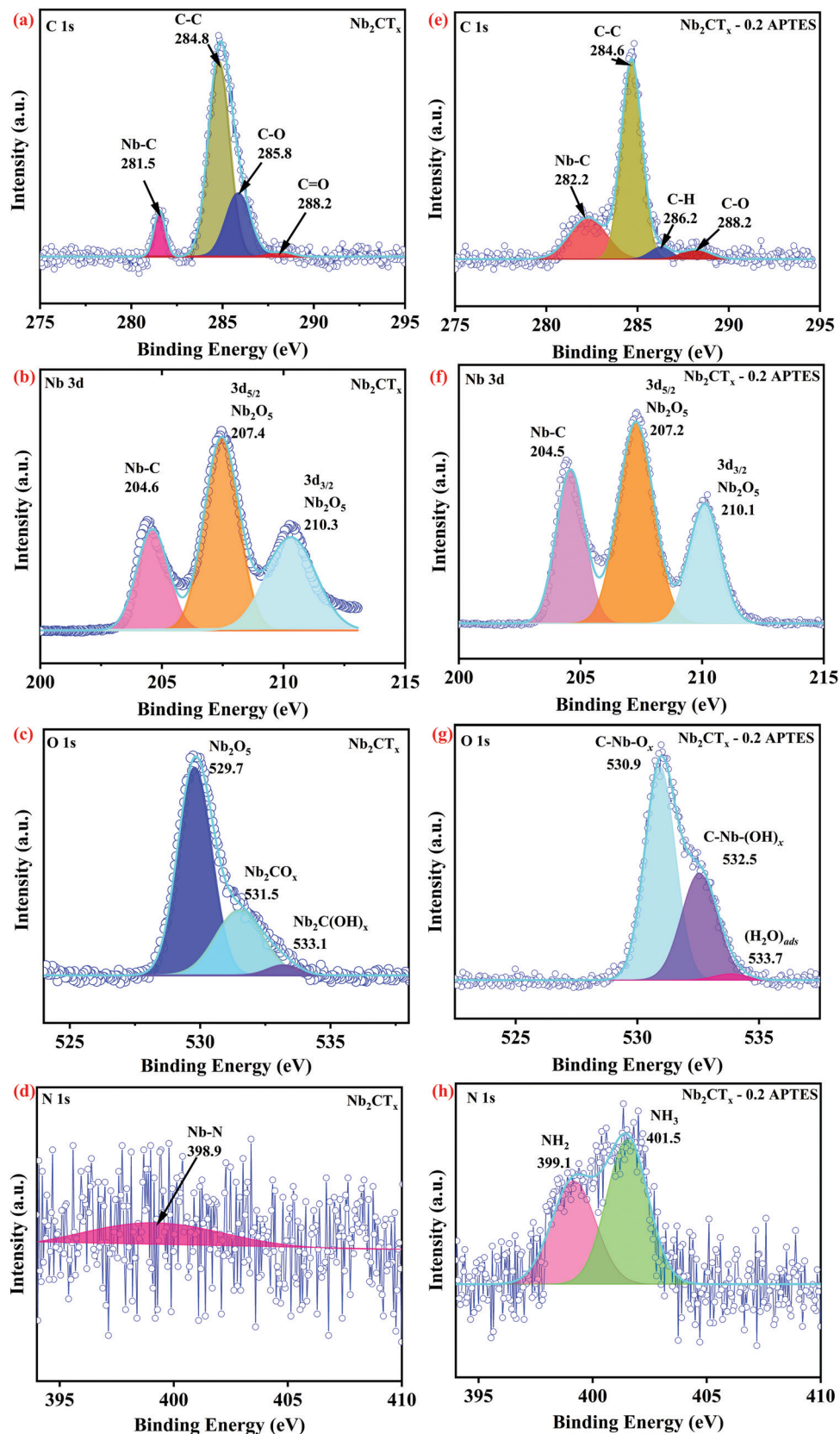


Fig. 2 XPS results of the as-synthesized Nb_2CT_x MXene (a–d) and Nb_2CT_x -0.2 APTES MXene (e–h).



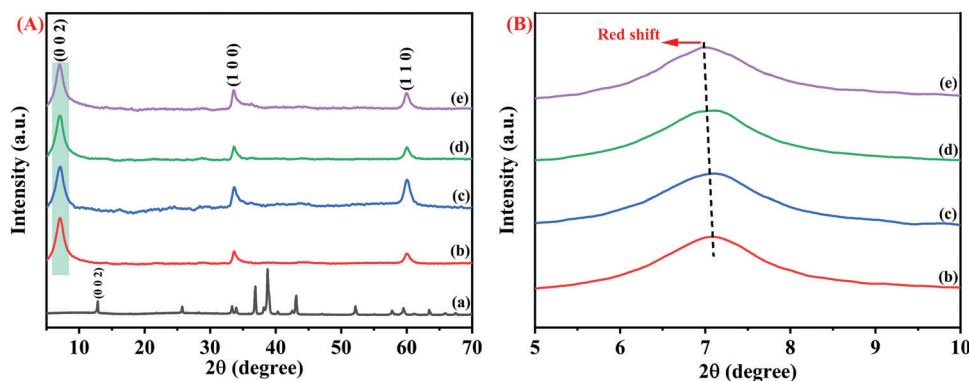


Fig. 3 (A) Full and (B) enlarged XRD of the Nb₂AlC MAX Phase (a), Nb₂CT_x MXene (b), Nb₂CT_x-0.1 APTES (c), Nb₂CT_x-0.2 APTES (d), Nb₂CT_x-0.3 APTES (e).

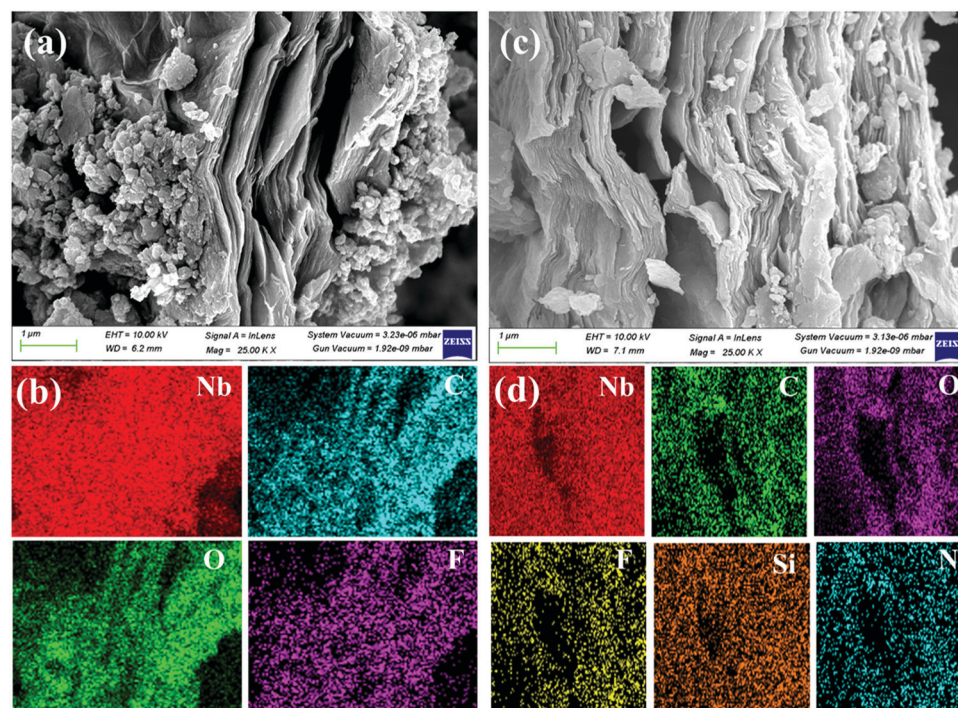


Fig. 4 FESEM and the corresponding elemental mapping of pristine Nb₂CT_x MXene (a and b) and Nb₂CT_x-0.2 APTES MXene (c and d).

functionalization increased. The homogeneous thick protective layer created by covalent contact *via* silylation processes accounts for this.

Nb₂CT_x-APTES MXene's stability was studied using zeta potential. From Fig. S6 (ESI[†]), it is observed that the negative zeta potential (−22.6 mV) on pristine MXene (due to negatively charged −OH group) got changed to positive zeta potential (25.5 mV) on 0.1 mL addition of APTES onto Nb₂CT_x MXene because of covalent interaction between APTES and MXene. It was observed that stability increases with an increase in the concentration of APTES molecules. However, an increase in the APTES concentration may decrease the conductivity of MXene sheets because of the lower conductivity of APTES.²⁴ Thus, a small fraction of APTES (0.2 mL) that can give satisfactory protection from degradation and maintaining MXene sheets conductivity was chosen for further studies.

Gas characterizations of Nb₂CT_x and Nb₂CT_x-0.2 APTES MXene

The as-synthesized Nb₂CT_x and Nb₂CT_x-APTES MXene were drop-casted onto the IDE and dried under a vacuum desiccator at room temperature for gas sensing studies. The drop-casted material will act as a conducting channel between the electrode gaps of IDE. Ohmic contact between the coated MXenes and Au/Ti electrodes was observed through *I*-*V* characteristics (between −2 and +2 V), as shown in Fig. S9 (ESI[†]). Gas sensing characteristics of the fabricated sensors were tested in an indigenously developed homemade sensing setup (Fig. S8, ESI[†]) at room temperature (~25 °C, 21% RH) for different target gases at different concentrations.

Fig. 5(a and b) show the dynamic sensing response of Nb₂CT_x MXene and Nb₂CT_x-0.2 APTES MXene for NO₂ gas at room temperature for different concentrations of 5–25 ppm with the help of dry air. The sensing response was calculated as

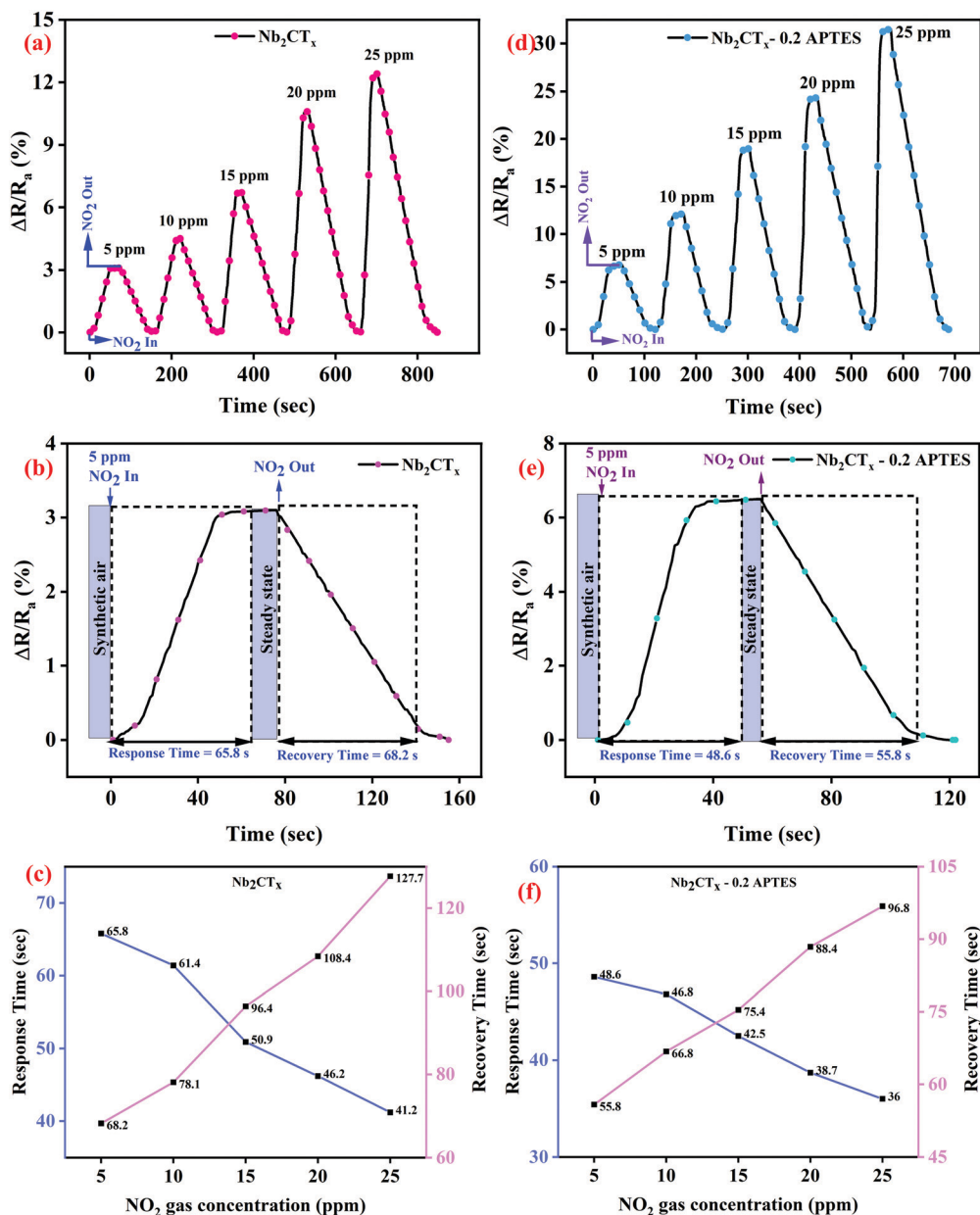


Fig. 5 Dynamic sensing response, response–recovery curves at different NO_2 gas concentrations of Nb_2CT_x MXene (a–c) and Nb_2CT_x -0.2 APTES MXene (d–f).

the relative change in the electrical resistance of the channel when injecting gas compared to the resistance of the baseline ($\Delta R/R_a$ (%)). The fabricated Nb_2CT_x and Nb_2CT_x -APTES sensors were stabilized under dry air before exposing to the target gases. A positive response was observed for both Nb_2CT_x and Nb_2CT_x -0.2 APTES MXenes toward NO_2 gas, which was attributed to the n-type behavior of the synthesized MXenes. The gas responses of 12.5% and 31.52% were observed toward Nb_2CT_x and Nb_2CT_x -0.2 APTES MXenes. The higher response toward APTES-functionalized MXene is due to increased C-lattice parameter and the attached $-\text{NH}_2$ groups. Increasing the C-lattice parameter helps to avail more surface area for the target gases to be adsorbed. Moreover, the amine functional groups on

APTES act as an electron acceptor that helps adsorb acidic gases such as NO_2 . Fig. S10 (ESI[†]) shows the dynamic sensing response of 0.1, 0.2, 0.3 mL APTES-functionalized Nb_2CT_x MXene. The gas sensing responses of 0.1, 0.2, and 0.3 mL APTES-functionalized Nb_2CT_x MXene samples were 22.5, 31.52, and 26.8%, respectively. It has been observed that the addition of APTES on Nb_2CT_x MXene enhances the sensing performance due to the increase in the C-lattice parameter and amine functionalization. However, at 0.3 mL APTES addition, the sensing response decreased compared to that at 0.2 mL APTES addition. Even more, the response time is also increased compared to 0.2 mL APTES-functionalized Nb_2CT_x MXene. This might be due to the increase in the Si–O–Si groups, which

hinders the conductivity of the MXene and hence the charge transfer between MXene and APTES molecules. Therefore, 0.2 mL APTES-functionalized Nb₂CT_x MXene has been used for further studies. The response and recovery time of the

fabricated sensor were determined based on the material's gas adsorption and desorption phenomena. The response and recovery times have been calculated as published elsewhere.³³ Nb₂CT_x-0.2 APTES MXene-based sensor showed better response ($t_{90} \sim 36$ s) and recovery time ($t_{10} \sim 96.8$ s) compared to the pristine Nb₂CT_x MXene-based sensor ($t_{90} \sim 41.2$ s and $t_{10} \sim 127.7$ s) at 25 ppm of NO₂ gas, as shown in Fig. 5(c and f). The fast response is due to the increased surface area and amine groups present on the Nb₂CT_x-0.2 APTES MXene. Higher recovery time compared to the response time is due to the chemisorption of NO₂ molecules on the sensing film.³⁴ Fig. S11 (ESI[†]) shows the sensing response of Nb₂CT_x and Nb₂CT_x-0.2 APTES MXene sensors at different relative humidity for 25 ppm NO₂ gas concentration. The response has been found to decrease with increasing humidity. The H₂O molecules interact with the adsorbed oxygen O₂⁻, thus decreasing the adsorption sites for NO₂ molecules. This decrease in the adsorption of NO₂ molecules suppresses the response of the sensors.³⁵ Pristine Nb₂CT_x MXene sensors strongly reduced its sensing performance at high humidity. However, the presence of the hydrophobic methoxy group possesses the anti-humidity property, which is attributed to the hydrophobic nature of the APTES layer on Nb₂CT_x MXene that helps to retain the sensing

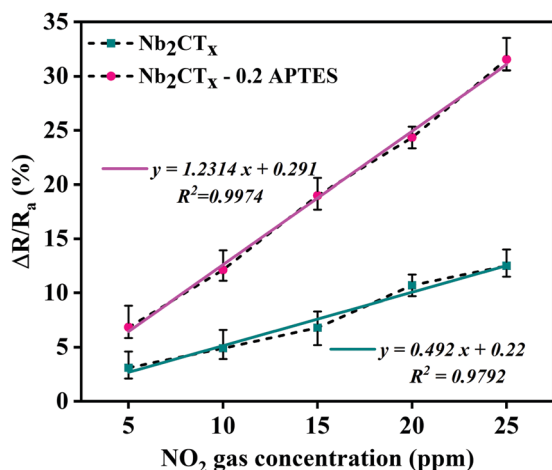


Fig. 6 The correlation of the response of the Nb₂CT_x and Nb₂CT_x-0.2 APTES-based sensor with NO₂ gas concentrations.

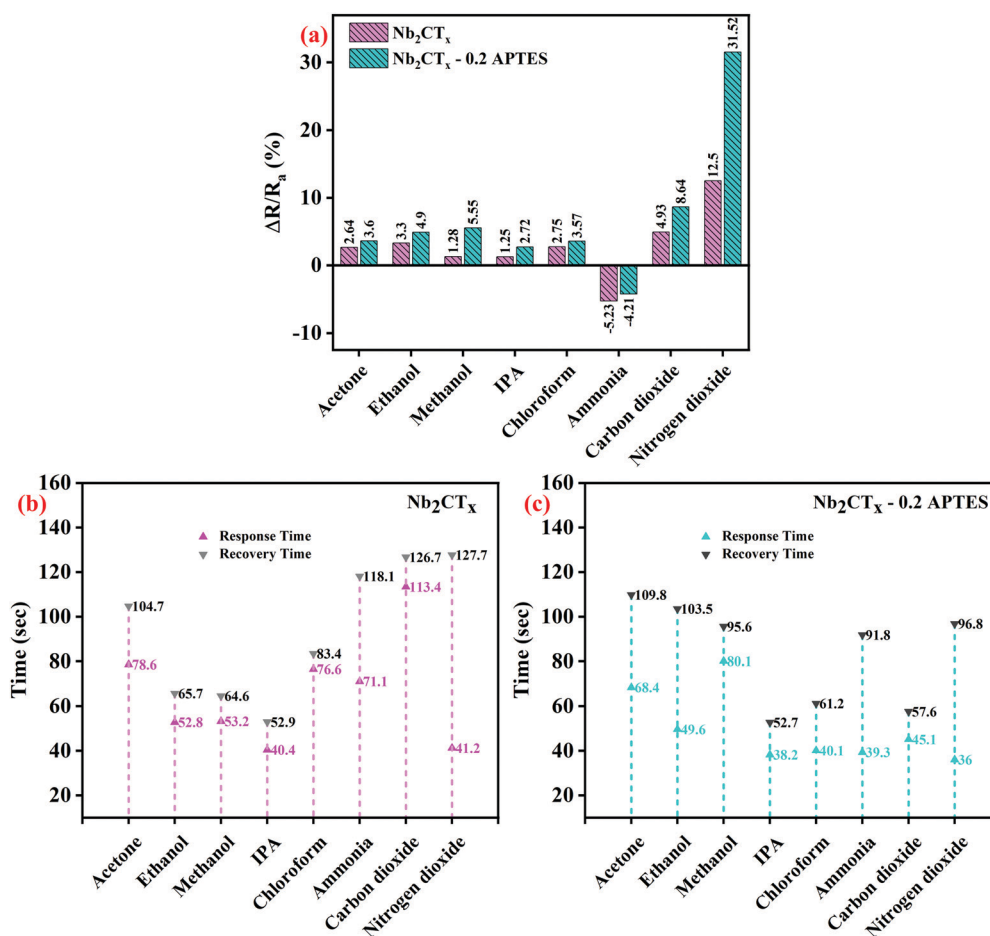


Fig. 7 (a) Selectivity of Nb₂CT_x and Nb₂CT_x-0.2 APTES based sensor and (b and c) their response–recovery time to different analytes.



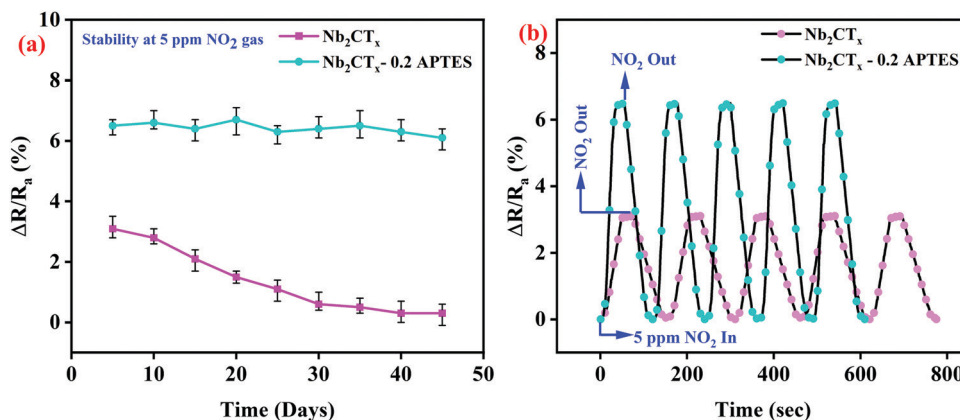


Fig. 8 (a) Long-term stability and (b) repeatability of Nb₂CT_x and Nb₂CT_x-0.2 APTES-based NO₂ gas sensor.

properties even under high humidity conditions.³⁶ It suggests that Nb₂CT_x-0.2 APTES has great potential in real-life gas sensing applications.

The sensitivity of both the fabricated sensors can be determined from the correlation graph between the sensing response and gas concentration, as shown in Fig. 6. The least-square method is used to fit the curve using the equation $y = mx + c$; y is the response, x is gas concentration, and m is the sensitivity. The sensitivities of Nb₂CT_x and Nb₂CT_x-0.2 APTES MXenes were found to be 0.492 and 1.2314 ppm⁻¹, respectively. The correlation coefficient R^2 (determines the linearity) is 0.9792 (Nb₂CT_x) and 0.9974 (Nb₂CT_x-0.2 APTES), which shows that Nb₂CT_x-0.2 APTES MXene had better sensitivity than that of pristine Nb₂CT_x MXene.

Fig. 7(a-c) shows the selectivity studies, response, and recovery times of the fabricated sensors tested against volatile organic compounds such as acetone, ethanol, methanol, isopropyl alcohol (IPA), chloroform, and gases such as ammonia and nitrogen dioxide gas at 25 ppm and carbon dioxide at 5000 ppm concentration. The dynamic response of the Nb₂CT_x MXene and Nb₂CT_x-0.2 APTES sensors are increased upon adding other reducing gases apart from ammonia, although these gases act as an electron donor. This is probably due to the ambipolar conductivity of the MXene. Both Nb₂CT_x and Nb₂CT_x-0.2 APTES sensors were highly selective toward NO₂

gas compared to other tested target species. Based on the above results, Nb₂CT_x-0.2 APTES MXene could be used for NO₂ sensors in daily life.

The Nb₂CT_x-0.2 APTES sensor showed long-term stability for 45 days with a minor reduction in the sensing response at 5 ppm NO₂ gas concentration, as shown in Fig. 8(a). The long-term stability is due to the formation of a homogeneous thick protective layer created by covalent contact *via* silylation processes on the Nb₂CT_x MXene, which stops the atmospheric air from interacting with the MXene surface.²⁴ Hydrophilic -NH₂ end groups on APTES helps in sensing the NO₂ gas, whereas, after 10 days, the sensing response of the Nb₂CT_x sensor got drastically decreased as it got degraded by interacting with atmospheric air. Fig. 8(b) shows the repeatability of both the fabricated sensors at 5 ppm NO₂ gas concentration at room temperature for several repeated tests (continuously 5 times). The sensors show an almost stable gas sensing response even after several repeated cycles; hence, the sensors offer good repeatability.

The limit of detection (LOD) and limit of quantification (LOQ) were calculated as per the formula reported elsewhere. LOD and LOQ of the fabricated Nb₂CT_x MXene sensors were found to be 15 ppb and 52 ppb, respectively, whereas, for Nb₂CT_x-0.2 APTES, the LOD and LOQ were calculated to be 3 ppb and 12 ppb, respectively. This confirms that the

Table 1 A comparative study on percentage response among the published 2D metal carbide MXenes-based chemiresistive sensor

S. no.	Materials used	Types of sensors	Operating temperature	Detection range	LOD	Analyte concentration (analyte)/response	Ref.
1	S-Ti ₃ C ₂ T _x	Chemiresistive	RT	1–50 ppm	Not reported	50 ppm (toluene)/–79.5%	37
2	V ₂ CT _x	Chemiresistive	RT	2–100 ppm	1.375 ppm	100 ppm (hydrogen)/24.35%	38
3	Ti ₃ C ₂ T _x -graphene	Chemiresistive	RT	10–50 ppm	Not reported	60 ppm (NH ₃)/6.77%	39
4	α-MoC _{1-x}	Chemiresistive	RT	0.125–5 ppm	Not reported	5 ppm (NO ₂)/–13.96%	40
5	V ₄ C ₃ T _x	Chemiresistive	RT	1–100 ppm	1 ppm	100 ppm (acetone)/2.65	41
6	PANI/Nb ₂ CT _x	Chemiresistive	RT	1–50 ppm	20 ppb	50 ppm (NH ₃)/205.4%	23
7	WO _{3-x} /APTES	Chemiresistive	RT	10–80 ppm	Not reported	10 ppm (ethanol)/19.1% 10 ppm (NO ₂)/7.9%	26
8	Ti ₃ C ₂ T _x /(γ-PGA)	Chemiresistive	RT	2–50 ppm	Not reported	50 ppm (NO ₂)/1127.3%	21
9	Alkalized V ₂ CT _x	Chemiresistive	RT	5–50 ppm	Not reported	50 ppm (NO ₂)/57.6%	22
10	Au@Te	Chemiresistive	RT	0.05–1 ppm	83 ppt	0.1 ppm (NO ₂)/3.18%	9
11	Nb ₂ CT _x	Chemiresistive	RT	5–25 ppm	15 ppb	25 ppm (NO ₂)/12.5%	This work
12	Nb ₂ CT _x -0.2 APTES	Chemiresistive	RT	5–25 ppm	3 ppb	25 ppm (NO ₂)/31.52%	This work



Nb_2CT_x -0.2 APTES sensor shows better sensing capabilities than the pristine Nb_2CT_x sensor.

The present work is compared with the available research articles and is formulated in Table 1. It is seen that the Nb_2CT_x -0.2 APTES sensor shows better sensing performance for its limit of detection, response recovery times, and selectivity compared to many other reported MXene-based sensors.

Sensing mechanism

Given the obtained gas sensing results, the following sensing mechanism is hypothesized for pristine and APTES-functionalized Nb_2CT_x MXene. Nb_2CT_x MXene synthesized from HF treatment possesses -F, -O, and -OH groups on the surface. However, after TMAOH treatment, Nb_2CT_x MXene is free from the -F surface groups, and the major functional groups are -OH and -O.⁴² The active surface terminations on Nb_2CT_x MXene contact oxygen

molecules and trap them from the air. Here, catalytic decomposition occurs, and O_2 molecules will turn into O atoms. O atoms and O_2 molecules may deprive electrons of the MXene via surface termination groups (*i.e.*, -OH and -O), resulting in oxygen ions such as O_2^- or O^- on the MXene surface. When NO_2 (oxidizing gas) is introduced into the testing chamber, it captures the O_2^- ions and creates many holes in MXene. Thus, due to the hindrance effect, the sensor's conductivity is decreased.

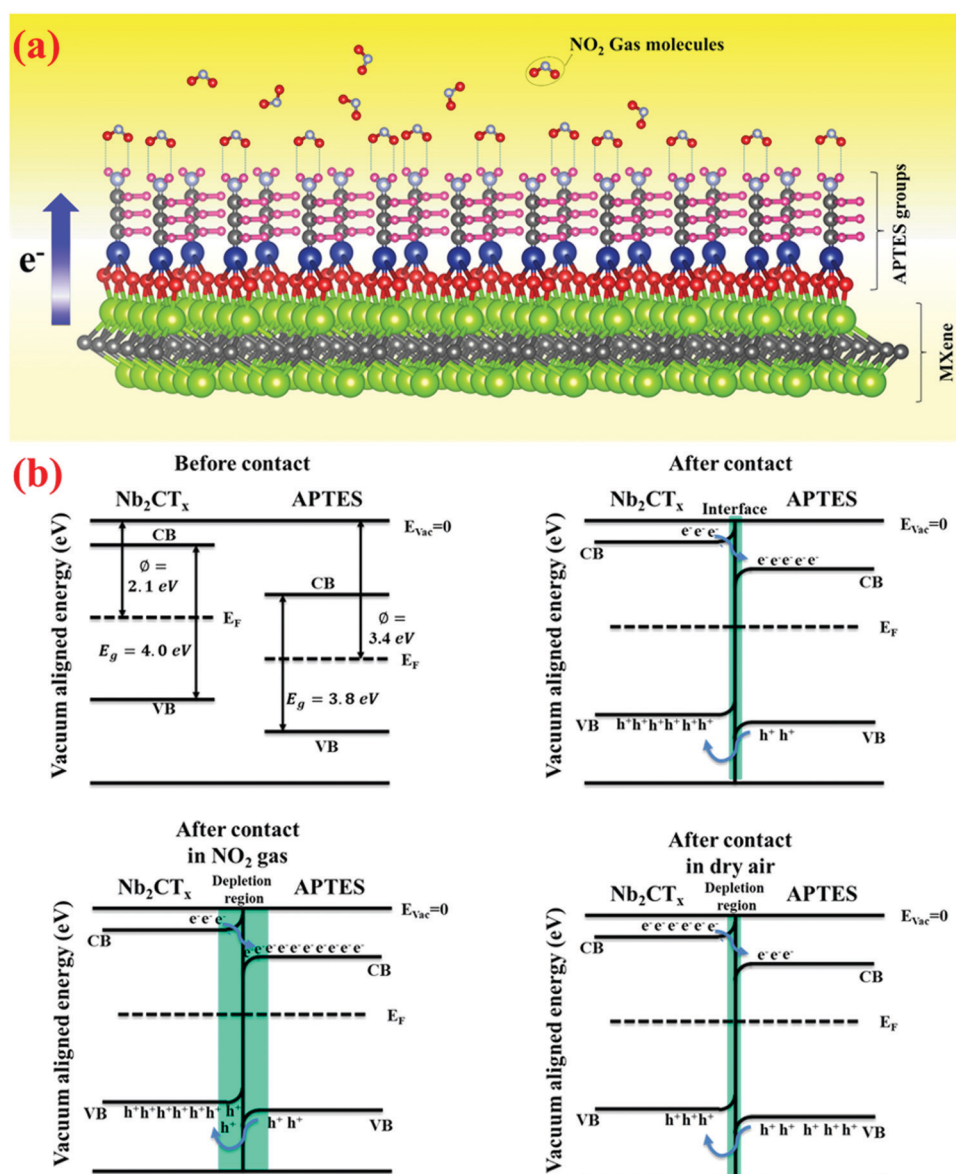
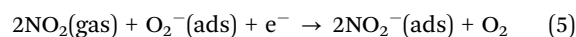
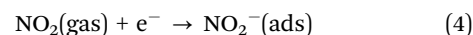
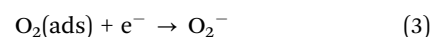
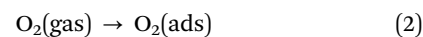


Fig. 9 (a) Sensing mechanism of Nb_2CT_x -0.2 APTES MXene for NO_2 gas, (b) energy band diagram of the Nb_2CT_x -0.2 APTES interface.



Further, APTES-functionalized Nb₂CT_x MXene sensing mechanism is explained using the energy band diagram shown in Fig. 9(b). Considering that Nb₂CT_x MXene is fully surface-terminated with –OH groups, the work function is reported to be 2.1 eV.⁴³ Meanwhile, the APTES work function and bandgap is reported to be 3.45 eV and 3.8 eV, respectively.²⁶ The bandgap is calculated from the Tauc plot and found to be 4.0 eV (Fig. S12, ESI†). When Nb₂CT_x MXene is functionalized with APTES, the electrons are transferred from Nb₂CT_x MXene to APTES to form the Fermi level. Due to this electron transfer, the energy bands bend, and a potential barrier occurs between Nb₂CT_x and APTES. Thus, APTES can capture electrons from Nb₂CT_x MXene when APTES-functionalized Nb₂CT_x MXene is kept under atmospheric air conditions. In APTES, electrons are trapped due to the presence of a significant potential barrier. This finding is consistent with the APTES-functionalized Nb₂CT_x sensor's higher resistance when compared to the pristine Nb₂CT_x sensor.

Because of unpaired electrons in oxygen atoms in NO₂ gas molecules, nitrogen dioxide possesses strong electron-withdrawing capabilities. Meanwhile, because it is a Lewis base in APTES, the –NH₂ group possesses significant electron-donating capabilities. Once the Nb₂CT_x-0.2 APTES sensor is tested for nitrogen dioxide gas, hydrogen bonds may be formed by the interaction between the –NH₂ group's H-atoms and unpaired electrons in O-atoms of nitrogen dioxide gas. Fig. 9(a) demonstrates how the NO₂ gas molecule reacts explicitly with the amine group of APTES to create a gas interaction between the self-assembled monolayers. When the electron transfer takes place from APTES to NO₂, it is balanced with the electron transfer from Nb₂CT_x MXene to establish a new equilibrium and expand the charge depletion zone. The introduction of NO₂ gas can further increase the charge depletion region till the saturation point. Later, when NO₂ gas is ejected, the depletion region decreases by increasing the conductivity back to its dry air conditions. The pre-stored electrons in APTES and the unique interaction between APTES and NO₂ may aid in achieving a low detection limit.

Conclusions

In summary, we have synthesized and fabricated a superiorly stable and selective NO₂ gas detector developed by APTES-functionalized Nb₂CT_x MXene. The covalent modification of Nb₂CT_x MXene with APTES showed better stability than pristine Nb₂CT_x MXene *via* silylation molecules and enabling the –NH₂ group. The electron-withdrawing property of NO₂ gas molecules accepts the electron from an amino group, a Lewis base in APTES. Meanwhile, APTES operates as an electron acceptor, and concurrently the transfer of electrons turns up from APTES to NO₂, supplementing the transfer of an electron from Nb₂CT_x to APTES to create a new equilibrium, resulting in an increased resistance of the sensor (n-type behavior). The Nb₂CT_x-0.2 APTES MXene sensor showed better sensing response (~2.5 times than the pristine Nb₂CT_x MXene sensor) with high sensitivity ($R^2 = 0.9974$) and stability (more than 45 days).

The fabricated sensors showed selectivity toward NO₂ gas compared to other target species. Thus, this study is promising for the long term, room temperature-operable MXene-based gas sensors and opens a new direction for the functionalization of MXenes.

Statistical analysis

All characterization results are reproducible. All selected areas of microscopy by SEM and HR-TEM are representative of the samples being analyzed. The SAED pattern of the prepared samples can be reproduced based on the same conditions as mentioned in the manuscript. Data shown in Fig. 5–8 represent the gas sensing characteristics, whose results are also reproducible. Statistical analysis was performed for the zeta potential measurements. One-way ANOVA was performed on all formulations to determine the statistical significance. Also, Origin 2021b (licensed version) and 3D Vesta (free version) software was used for plotting.

Author contributions

N. K. Arkoti: conceptualization, methodology, investigation, validation, formal analysis, data curation, writing – original draft, writing – review & editing. K. Pal: conceptualization, supervision, writing – review & editing, funding acquisition.

Conflicts of interest

There are no conflicts to declare.

Acknowledgements

The authors would like to thank the MHRD, Government of India, for providing financial support to carry out this work. The authors also would like to thank the Department of Metallurgy and Materials Engineering, IIT Roorkee, for providing an HR-TEM facility.

References

- 1 Z. Meng, R. M. Stolz, L. Mendecki and K. A. Mirica, *Chem. Rev.*, 2019, **119**, 478–598.
- 2 Z. Yang, D. Zhang and H. Chen, *Sens. Actuators, B*, 2019, **300**, 127037.
- 3 Y. Zhou, G. Liu, X. Zhu and Y. Guo, *Sens. Actuators, B*, 2017, **251**, 280–290.
- 4 P. Srinivasan, M. Ezhilan, A. J. Kulandaisamy, K. J. Babu and J. B.-B. Rayappan, *J. Mater. Sci.: Mater. Electron.*, 2019, **30**, 15825–15847.
- 5 S. J. Kim, H. J. Koh, C. E. Ren, O. Kwon, K. Maleski, S. Y. Cho, B. Anasori, C. K. Kim, Y. K. Choi, J. Kim, Y. Gogotsi and H. T. Jung, *ACS Nano*, 2018, **12**, 986–993.
- 6 E. Lee and D.-J. Kim, *J. Electrochem. Soc.*, 2020, **167**, 037515.
- 7 X. Liu, T. Ma, N. Pinna and J. Zhang, *Adv. Funct. Mater.*, 2017, **27**, 1702168.
- 8 M. G. Stanford, K. Yang, Y. Chyan, C. Kittrell and J. M. Tour, *ACS Nano*, 2019, **13**, 3474–3482.



- 9 Z. Yuan, Q. Zhao, C. Xie, J. Liang, X. Duan, Z. Duan, S. Li, Y. Jiang and H. Tai, *Sens. Actuators, B*, 2022, **355**, 131300.
- 10 K. Rath and K. Pal, *ACS Appl. Mater. Interfaces*, 2020, **12**, 38365–38375.
- 11 W. Liu, D. Gu and X. Li, *ACS Appl. Mater. Interfaces*, 2021, **13**, 20336–20348.
- 12 M. Naguib, M. W. Barsoum, Y. Gogotsi, M. Naguib, M. W. Barsoum, Y. Gogotsi and A. Y.-J. Gogotsi, *Adv. Mater.*, 2021, **33**, 2103393.
- 13 Y. Liu, E. Li, Y. Yan, Z. Lin, Q. Chen, X. Wang, L. Shan, H. Chen and T. Guo, *Nano Energy*, 2021, **86**, 106118.
- 14 K. Sarang, X. Zhao, D. Holta, H. Cao, K. Arole, P. Flouda, E. S. Oh, M. Radovic, M. J. Green and J. L. Lutkenhaus, *ACS Appl. Energy Mater.*, 2021, **4**, 10762–10773.
- 15 L. Jiang, J. Duan, J. Zhu, S. Chen and M. Antonietti, *ACS Nano*, 2020, **14**, 2436–2444.
- 16 K. Meidani, Z. Cao and A. Barati Farimani, *ACS Appl. Nano Mater.*, 2021, **4**, 6145–6151.
- 17 Y. Pei, X. Zhang, Z. Hui, J. Zhou, X. Huang, G. Sun and W. Huang, *ACS Nano*, 2021, **15**, 3996–4017.
- 18 M. Wu, Y. An, R. Yang, Z. Tao, Q. Xia, Q. Hu, M. Li, K. Chen, Z. Zhang, Q. Huang, S. H. Ma and A. Zhou, *ACS Appl. Nano Mater.*, 2021, **4**, 6257–6268.
- 19 C. Fan, J. Shi, Y. Zhang, W. Quan, X. Chen, J. Yang, M. Zeng, Z. Zhou, Y. Su, H. Wei and Z. Yang, *Nanoscale*, 2022, **14**, 3441–3451.
- 20 A. Junkaew and R. Arróyave, *Phys. Chem. Chem. Phys.*, 2018, **20**, 6073–6082.
- 21 Q. Zhao, D. Sun, S. Wang, Z. Duan, Z. Yuan, G. Wei, J. L. Xu, H. Tai and Y. Jiang, *ACS Sens.*, 2021, **6**, 2858–2867.
- 22 Y. Zhang, Y. Jiang, Z. Duan, Q. Huang, Y. Wu, B. Liu, Q. Zhao, S. Wang, Z. Yuan and H. Tai, *Sens. Actuators, B*, 2021, **344**, 130150.
- 23 S. Wang, Y. Jiang, B. Liu, Z. Duan, H. Pan, Z. Yuan, G. Xie, J. Wang, Z. Fang and H. Tai, *Sens. Actuators, B*, 2021, **343**, 130069.
- 24 J. Ji, L. Zhao, Y. Shen, S. Liu and Y. Zhang, *FlatChem*, 2019, **17**, 100128.
- 25 H. Riazi, M. Anayee, K. Hantanasirisakul, A. Arabi Shamsabadi, B. Anasori, Y. Gogotsi, M. Soroush, H. Riazi, A. A. Shamsabadi, M. Soroush, M. Anayee, K. Hantanasirisakul, B. Anasori and Y. A. Gogotsi, *Adv. Mater. Interfaces*, 2020, **7**, 1902008.
- 26 M. Tomić, Z. Fohlerova, I. Gràcia, E. Figueras, C. Cané and S. Vallejos, *Sens. Actuators, B*, 2021, **328**, 129046.
- 27 G. Zhang, T. Wang, Z. Xu, M. Liu, C. Shen and Q. Meng, *Chem. Commun.*, 2020, **56**, 11283–11286.
- 28 K. Maleski, C. E. Shuck, A. T. Fafarman and Y. Gogotsi, *Adv. Opt. Mater.*, 2021, **9**, 1–8.
- 29 K. Rath and K. Pal, *Nanotechnology*, 2020, **31**, 135502.
- 30 M. Wu, M. He, Q. Hu, Q. Wu, G. Sun, L. Xie, Z. Zhang, Z. Zhu and A. Zhou, *ACS Sens.*, 2019, **4**, 2763–2770.
- 31 Z. U. Din Babar, J. Fatheema, N. Arif, M. S. Anwar, S. Gul, M. Iqbal and S. Rizwan, *RSC Adv.*, 2020, **10**, 25669–25678.
- 32 I. J. Echols, D. E. Holta, V. S. Kotasthane, Z. Tan, M. Radovic, J. L. Lutkenhaus and M. J. Green, *J. Phys. Chem. C*, 2021, **125**, 13990–13996.
- 33 S. Bag and K. Pal, *Sens. Actuators, B*, 2020, **303**, 127115.
- 34 S. Y. Cho, K. M. Cho, S. Chong, K. Park, S. Kim, H. Kang, S. J. Kim, G. Kwak, J. Kim and H. T. Jung, *ACS Sens.*, 2018, **3**, 1329–1337.
- 35 S. Gasso, M. K. Sohal and A. Mahajan, *Sens. Actuators, B*, 2022, **357**, 131427.
- 36 W. Liu, L. Xu, K. Sheng, C. Chen, X. Zhou, B. Dong, X. Bai, S. Zhang, G. Lu and H. Song, *J. Mater. Chem. A*, 2018, **6**, 10976–10989.
- 37 S. N. Shuvo, A. M. Ulloa Gomez, A. Mishra, W. Y. Chen, A. M. Dongare and L. A. Stanciu, *ACS Sens.*, 2020, **5**, 2915–2924.
- 38 E. Lee, A. Vahidmohammadi, Y. S. Yoon, M. Beidaghi and D. J. Kim, *ACS Sens.*, 2019, **4**, 1603–1611.
- 39 S. H. Lee, W. Eom, H. Shin, R. B. Ambade, J. H. Bang, H. W. Kim and T. H. Han, *ACS Appl. Mater. Interfaces*, 2020, **12**, 10434–10442.
- 40 S. Y. Cho, J. Y. Kim, O. Kwon, J. Kim and H. T. Jung, *J. Mater. Chem. A*, 2018, **6**, 23408–23416.
- 41 W. N. Zhao, N. Yun, Z. H. Dai and Y. F. Li, *RSC Adv*, 2020, **10**, 1261–1270.
- 42 J. Luo, E. Matios, H. Wang, X. Tao and W. Li, *InfoMat*, 2020, **2**, 1057–1076.
- 43 Y. Liu, H. Xiao and W. A. Goddard, *J. Am. Chem. Soc.*, 2016, **138**, 15853–15856.

